Electrochimica Acta 362 (2020) 137200

Contents lists available at ScienceDirect

Electrochimica Acta

journal homepage: www.elsevier.com/locate/electacta

Upcycling of polyurethane into iron-nitrogen-carbon electrocatalysts active for oxygen reduction reaction

Giorgia Daniel[a], Tomasz Kosmala[a], Maria Chiara Dalconi[b], Luca Nodari[c], Denis Badocco[a], Paolo Pastore[a], Alessandra Lorenzetti[d], Gaetano Granozzi[a], Christian Durante[a,*]

[a] Department of Chemical Sciences, University of Padova, via Marzolo 1, Padova 35131, Italy
[b] Department of Geoscience, University of Padova, via Gradenigo 6, Padova 35131, Italy
[c] Istituto di Chimica della Materia Condensata e di Tecnologie per l'Energia, CNR-ICMATE, INSTM, C.so Stati Uniti 4, Padova 35127, Italy
[d] Departement of Industrial Engineering, University of Padova, via Marzolo, 9, Padova 35131, Italy

ARTICLE INFO

Article history:
Received 26 May 2020
Revised 26 September 2020
Accepted 26 September 2020
Available online 6 October 2020

Keywords:
Polyurethane
Nitrogen doped carbon
Oxygen reduction reaction
Fe-N-C
Fuel cell
H_2O_2

ABSTRACT

World plastic production has increased since industrial-scale production began in the 1940s and while large amount of thermoplastic polymers can be effectively recycled and re-used, undifferentiated polymers or thermoset polymers cannot, and as a result, most of these raw materials end up in landfill or energy recovery in incinerators. The synthesis of carbon nanomaterials from conversion of waste polymers is an alternative, promising approach owing to the high added-value of these products. In particular, novel carbon materials, could translate into interesting and cheap material for the catalytic reduction of oxygen (ORR), a fundamental reaction for the production of H_2O_2 or in fuel cell and metal air batteries.

This paper presents the synthesis of iron-nitrogen-carbon (Fe-N-C) electrocatalysts starting from a mix of polyethylene (PE) and polyurethane (PU) by adding $FeCl_3$ as an iron source for promoting Fe-N_x sites formation. The two polymers were mixed according to a solvent assisted process employing p-xylene or with a solvent free process using a Brabender plastograph. The blend of thermoplastic and thermoset polymers was converted into Fe-N-C materials in a two-step pyrolysis, where the temperature of second pyrolysis showed to sensitively affect the chemical and textural properties of the resulting material. Depending on the temperature, and initial PE content, the surface area ranges between 195 and 479 $m^2\ g^{-1}$, with a preferential formation of micropores. XPS analysis confirmed that the employment of PU leads to the formation of nitrogen functional groups and Fe-N_x sites, while XRD investigation in heating chamber allowed to follow the formation Fe_3C, Fe_2O_3, γ-Fe and α-Fe with temperature rises between 700–1000°C. The new Fe-N-C catalysts were characterized by linear sweep voltammetry at ring disk electrode showing interesting activity for the ORR in both acid and alkaline electrolyte and a selectivity for H_2O_2 which deeply depends on the type of electrolyte as well as on nitrogen content and on the surface area of the samples.

1. Introduction

Plastic is an important and ubiquitous material in our daily life, and it is often the unique choice when it is necessary to assure lightness as in cars or planes [1], insulation ability as in building [2] or biocompatibility as in food packaging [3] and in biomedical devices [4]. However, too often the way plastics are currently produced, used and discarded fails to capture the economic benefits of a more "circular" approach and harms the environment. In 2014 in Europe, 25.8 million tons of post-consumer plastics waste ended up in the official waste streams. 69.2% was recovered through recycling and energy recovery processes, while 30.8% still went to landfill [5]. Conversely to thermoplastic, thermoset polymers cannot be recycled and re-used, and as a result, they end up in landfill or energy recovery through incinerators, so contributing to the global carbon footprint. Incineration can be used to transfer waste plastic into energy; however, the loss of potential chemical resources and the negative public acceptance has limited the application of this solution. Landfill is even less desirable in a zero-waste philosophy and circular economy. For example, today, in USA and Europe, most polyurethane (PU)

* Corresponding author.
E-mail address: christian.durante@unipd.it (C. Durante).

https://doi.org/10.1016/j.electacta.2020.137200

thermal insulation scrap and waste materials are still disposed of in landfills, after compacting them into brickets with a density of approximately 500 kg/m^3 [5]. Plastics are mainly composed of carbon and hydrogen; therefore, converting waste plastics into valuable chemicals or materials is an ideal alternative, which can not only solve the problem of waste plastic disposal, but also create high-value-added products. The feedstock recycling of polymers has been extensively studied in the past, but have not become largely used yet due to limited economic viability.

The synthesis of carbon nanomaterials is an alternative, promising approach owing to the high added-value of these products. Up to now, many studies have been conducted on converting virgin or waste plastics, including polypropylene [6], polyethylene (PE) [7,8], polystyrene [9] and polyurethane (PU) [10,11], into carbon nanomaterials with different morphologies and structure, such as carbon nanotubes [12], graphene [13,14], and porous carbons [15–18]. Among several routes, polymers are converted into carbon materials by pyrolysis [19,20] employing transition metal oxides as catalysts, which serve for controlling the size of carbon spheres [13] and to prompt the degradation of polymers into aromatic structures [6,21]. Waste-derived carbon nanomaterials can find application in different fields including biomedical field [22], catalysis [19], and energy conversion and storage devices [15], such as fuel cell, batteries [20] and electrochemical supercapacitors [15,16]. Therefore, plastic waste conversion to carbon nanomaterials with improved physico-chemical properties and morphology is a new potential application for recycling thermoset waste polymers or undifferentiated plastic materials.

Among different applications, carbon-based nanomaterials doped or co-doped with nitrogen or other heteroatoms showed interesting electroactivity in oxygen reduction reaction (ORR) [23–28] ORR may proceed according two ways leading to H_2O or H_2O_2 through a tetra-electronic Eq. (1)) or a bi-electronic mechanism (Eq. (2,(3)), respectively.

$$O_2 + 4H^+ + 4e^- \leftrightarrow 2H_2O \qquad E^o = 1.23\ V \tag{1}$$

$$O_2 + 2H^+ + 2e^- \leftrightarrow H_2O_2 \quad E^o = 0.69\ V \tag{2}$$

$$H_2O_2 + 2H^+ + 2e^- \leftrightarrow 2H_2O \qquad E^o = 1.76\ V \tag{3}$$

Both reduction pathways are kinetically hindered, therefore, catalysts must be used to boost the rate of the reduction process. The development of electrocatalysts able at catalysing the oxygen reduction to H_2O_2 is a green alternative to the anthraquinone process that counts for a global production of H_2O_2 that exceeds 3 million tons for a value of 4.2 Billion US$, and the global demand is projected to rise at a rate of almost 4-5%/year [29]. On the other hand, catalysts that can promote the direct four-electron pathway, where O_2 is reduced directly to water, are highly desirable for the cathode side of proton exchange membrane fuel cell (PEMFC), whose market is expected to witness a growth in the next future. At present Pt [30–33] and Pt alloys [34,35] in nanostructure sizes represent the only valid catalysts for PEMFC [36]. However, Pt suffer from high cost and low availability and has been labelled as a *critical raw material*; in fact, according to the Johnson Matthey February report 2020, which considers total supply and total gross demand, the balance is negative by – 203K oz [37]. Therefore, the widespread commercialization of PEMFC will probably need to discover new Pt-free catalysts, i.e., catalysts based on non-Pt-group metals (non-PGM). Among non-PGM, iron-nitrogen carbon-based materials (Fe-N-C) are the most interesting system in terms of activity and stability. The nature of the active sites in Fe-N-C is still under debate, however there is a general consensus on the role of Fe-N_x centers to catalyze ORR [38], even though other co-catalyst such as Fe_3C and metallic Fe NPs encapsulated by a carbon shell are supposed to assist the tetra-electronic reduction mechanism of oxygen in acid media [39]. Furthermore, the activity is not only linked to the downsized active sites, but strongly depends on their micro-mesoporous environment [40]. In fact, some Fe-N_x moieties hosted in inaccessible micropores do not contribute to the ORR activity and they are often inactive [41].

Fe-N-C catalysts are usually synthetized by heat treatment or ball milling of a carbon material with an iron complex, or by the pyrolysis of suitable precursors containing carbon, nitrogen and iron [23,25] such as MOF [42–45], polymers [46–48] or biomasses [23,49–51]. Therefore, it is natural to assume that in the frame of a circular economy, the conversion of waste plastic into added-value carbon materials is an attractive alternative to solve both the cost synthesis and procurement of the precursors and the environmental problems [52].

In this work, PE and PU polymers are decomposed via two step pyrolysis and an activation treatment into functional micro-mesoporous Fe-N-C materials and are tested as electrocatalysts for ORR. The employment of a mixture of PE and PU was considered for mimicking the condition of undifferentiated polymer waste, which represent the main and more challenging innovation of this paper. Thermoset PU was chosen because it is not recyclable and because it plays as both carbon and nitrogen source, while $FeCl_3$ was used to form Fe-N_x active sites. Furthermore, PE was adopted as dispersing matrix for obtaining a homogeneous mixing of all components in both a solvent free extrusion procedure and in a solvent assisted mixing of components. It is in plain view that many other thermoplastic polymers can be likewise adopted. The effect of the synthesis temperature on the textural and chemical properties of the obtained Fe-N-C materials was carefully investigated. Furthermore, the electrocatalytic performances of the resulting materials in the ORR were rationalized on the basis of key parameters such as surface area, micro- and meso-pore volume and surface and nitrogen or iron content.

2. Materials and methods

2.1. Synthesis of Fe-N-C

Fe-N-C materials were prepared by pyrolysis of a blend of polymers ad an iron salt according to a sequence of steps reported in Fig. 1. There are several examples in literature were PU scaffold is used as sacrificial template [54–57], differently from this investigation were PU plays as both carbon and nitrogen source. 5 g of low-density polyethylene pellets (LDPE) were solubilized in 53 mL of *p*-xylene heated at 115°C under vigorous stirring to help the homogenization (Fig. 1a). 4 g of polyurethane powder (PU, see SI for synthesis details) and 0.3 g of $FeCl_3 \bullet 6H_2O$ were then sequentially added and mechanically mixed obtaining a red-like blend. The iron precursor was added with the aim to promote the formation of Fe-N_x sites, which are active for the reduction of molecular oxygen. The quantities of both PU and $FeCl_3$ were considered based on the maximum amount dispersible in the PE/p-xylene solution according to an empirical evaluation. The obtained mixture was then dried on a heating plate at 60°C and then transferred in a vacuum quartz test tube, which was closed from one side, while a cone 26 was weld on the other side for allowing the connection with the inlet and the outlet lines (Fig. 1b). The mixture was subjected to consecutive vacuum/nitrogen cycles in a Schlenk line for completely remove *p*-xylene, water and oxygen, which would sensitively lower the final carbon yield because of the precursor's bun off. The glass tube was subsequently insert in a vertical tubular furnace avoiding any exposure of the blend to the atmosphere, that was ensured by adopting a bubbler-like stopper as the one in Fig. 1c. The pyrolysis of the blend was carried out in two steps, because the direct pyrolysis at high temperature entails the forma-

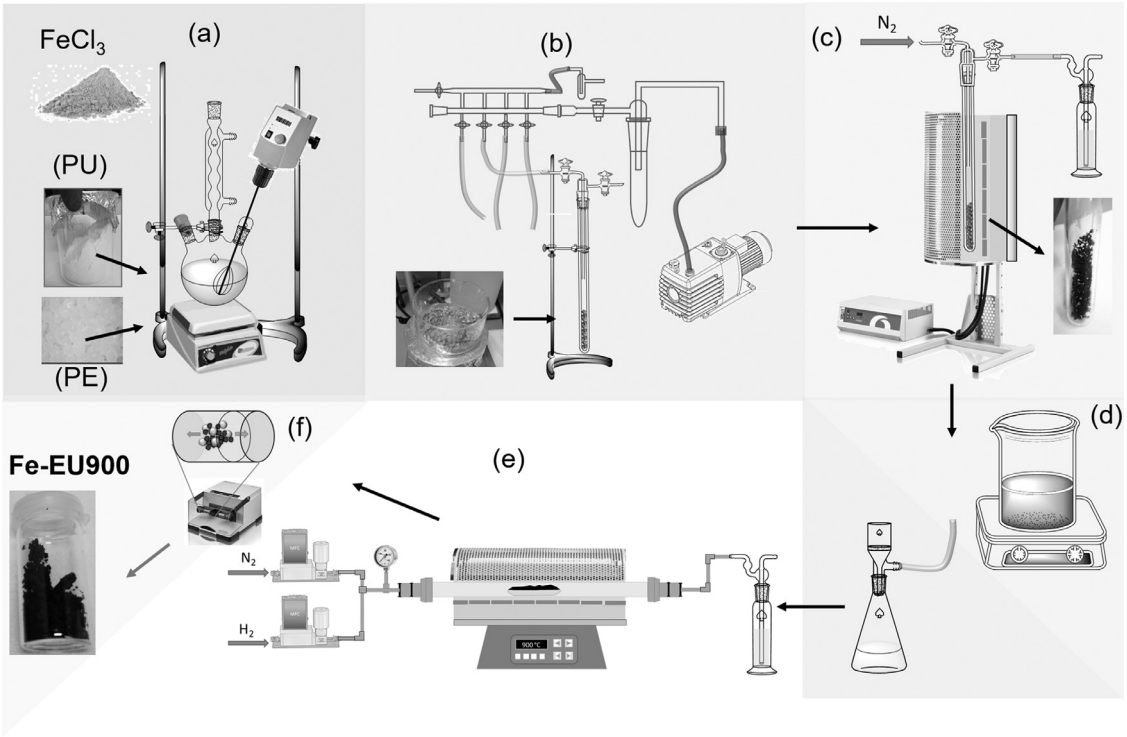

Fig. 1. Different stages of Fe-N-C material synthesis (a) mechanical mixing of polymers and $FeCl_3$, (b) drying and degassing of polymer blend, (c) double step pyrolysis, (d) acid wash in H_2SO_4 at 100°C and filtration on nylon membrane, (e) thermal activation in H_2 flow, (f) ball milling.

tion of a consistent fraction of liquid phase, which drastically decrease the carbon yield due to the burn off and to its crossover into the scrubber line, positioned at the exit of the furnace. Therefore, light pyrolysis was firstly performed at 500°C for 30 min, where the vertical alinement of the quartz tube inside the furnace enabled a reflux of light polycyclic aromatic hydrocarbons, which are involved in "ring-ring" condensation to form larger polycyclic aromatic hydrocarbons [53]. The resulting yellow-red wax and foam-like carbon were separated and only the latter fraction was subject to a second pyrolysis under nitrogen atmosphere at different temperatures and thoroughly examined.

The viscous liquid fraction contains a mixture of olefins, such as ethylbenzene, annulene, toluene, benzene, naphthalene, phenanthrene, and it was manually scraped with a spatula avoiding touching the foam-like carbon [54]. Then, the carbon was collected overturning the reaction tube. Four different temperature were tested: 700, 800, 900 and 1000°C, and the resulting materials were labelled as Fe-EU700, Fe-EU800, Fe-EU900 and Fe-EU1000, respectively. A further sample was prepared without the addition of $FeCl_3 \bullet 6H_2O$ and another one without LDPE named as EU900 and Fe-U900, respectively. The powders were then activated by acid washing in a 0.5 M H_2SO_4 solution at 100°C for 15 min, after which the mixture was filtered on a nylon nanometric filter (GVS, nylon 0.2 mm, 47 mm membrane diameter) and washed several times with milli-Q water and ethanol. The samples were subsequently dried at 80°C for one night and afterwards heated in a tubular furnace at 900°C in a reducing H_2 atmosphere (8% H_2 in H_2/N_2 mixture) for 2 h (Fig. 1e). The resulting powder was then ground by vibro-milling (Retsch MM 400, 2 steps of 20 min / 20-25 Hz) and recovered in a glass vial.

A solvent free procedure was also attempted by mixing PE, PU and $FeCl_3$ with a Brabender plastograph, which is a device for the continuous observation of torque in the shearing of a polymer at different temperatures and shear rates. It also allows the vigorous mixing of small quantities of thermoplastic polymers without resorting to larger machines such as extruders. The materials are generally introduced through a hopper into the chamber, where they are heated and subjected to cutting forces by passing between two counter-rotating screws, rotating at different speeds. For obtaining a good mixing it is important to careful control temperature and screw speed, therefore the two parameters were tuned step by step. While thermoplastic polymer can be easily mixed with other additives and extruded, thermoset polymers such as polyurethane cannot. Therefore, the only way to obtain a homogeneous mixture is to use a high polyolefins/polyurethane ratio were PU can be considered indeed an additive. Bearing this in mind, a first amount of PE (5 g) was initially inserted setting a temperature of 150°C and a rotation rate of 100 rpm, afterwards a second amount was added, and the temperature was decreased to 140°C, keeping the rotation rate at 100 rpm to favor the fusion and mixing of PE. Then, 20 more grams of PE were added in two different slots, setting the temperature again at 150°C and the mixing was kept constant until obtaining a complete fused compound. 4 g of PU were then poured into the plastograph, while the speed was drastically reduced to 30 rpm for avoiding any puffs and for obtaining a good mixture. Eventually, 0.17 g of $FeCl_3$ were added, while the rotation speed was increased to 50 rpm and maintained constant for 5 min. It is in plain view that the solvent free approach in limited by the amount of PU that can be effectively inserted with a Pu/PE ratio of 4/30, which is much lower than the 4/5 employed in the solvent assisted approach. For the same reason also the $FeCl_3$ content needed to be reduced. In Fig. S1 are reported the extruded product along with the torque moment and the temperature as a function of time, were each spike represents the different material additions. The extruded product was then pyrolyzed in a two-step process and activated as it was done for Fe-EU800, and the resulting catalyst was named as Fe-EU800B.

2.2. Instrumentation and experimental details

Textural properties were determined from nitrogen adsorption/desorption isotherms performed at 77 K using a Micromerit-

ics ASAP2020. The surface area was determined by the desorption curve in a multipoint BET (Brunaumer-Emmett-Teller) analysis, whereas pore distribution was analyzed with a cylindric/spherical pore QSDFT adsorption model. Elemental analysis (EA) was carried out using a Thermo Scientific Flash 2000. Transmission electron microscopy (TEM) images were obtained by using a FEI Tecnai G2 microscope operating at 100 kV. Scanning electron microscopy (SEM) images were performed with a Zeiss Sigma HD FE-SEM. X-ray photoemission spectroscopy (XPS) measurements were performed in an UHV chamber (base pressure $< 5 \times 10^{-10}$ mbar), equipped with a double anode X-ray source (Omicron DAR-400) and a hemispherical electron analyzer (Omicron EIS-125) at room temperature; a non-monochromatized Mg-Kα radiation (hν = 1253.6 eV) and pass energies of 50 eV and 20 eV for the survey and the single spectral windows, respectively, were used. To perform XPS measurements, 2.5 mg of the MC powders were dispersed in 1 mL of ethanol by sonication for 10 min; the solutions were then drop-casted onto polycrystalline copper (with a diameter of 6 mm). XRD measurements were acquired by using a Panalytical X'Pert Pro diffractometer equipped with a Co anode X-ray tube (40 kV, 40 mA), Bragg–Brentano optical module, and X'Celerator detector. Diffraction patterns were collected in the 2θ = 2°- 80° range, with 2θ = 0.0338° virtual step size, counting an equivalent time of 100 s per step. *In-situ* high temperature diffraction measurements were performed with an Anton Paar HTK-16 heating system attached to the diffractometer. During measurements the heating chamber was fluxed with 1 L min^{-1} N_2 to prevent oxidation of the sample. High temperature XRD patterns were collected in the 15°-80° 2θ-range, with a virtual step size of 0.0338° 2θ, counting an equivalent time of 80 s per step. Powder sample was deposited on a Pt-strip and heated up to 700°C with a heating rate of 10°C/min. First diffraction data were collected after 40 min of thermal equilibration time. XRD patterns were then collected at 800°C, 900°C and 1000°C using a heating rate of 5°C/min and waiting 20 min for thermal equilibration before data collection.

An Agilent Technologies 7700x ICP-MS was employed for inductively coupled plasma mass spectrometry analysis. The samples (5 mg) for ICP analysis were treated using a microwave system CEM EXPLORER SP.D PLUS at a heating rate of 40°C/min from room temperature to 220°C with a pressure of 400 psi and a power of 300 W.

Room temperature Mössbauer spectra were collected by means of a conventional constant acceleration spectrometer mounting an ^{57}Co source, nominal strength 1850 MBq. The hyperfine parameters isomer shift (δ), quadrupole splitting (Δ), half linewidth at half maximum (Γ_+), were expressed in mm s^{-1} while internal magnetic field (B) in Tesla (T) and the relative area (A) in %, were obtained by means of standard least-squares minimization techniques.

2.3. Electrochemical tests

Voltammetric measurements were performed by using an Autolab Model 101 N potentiostat/galvanostat in a three-electrode, thermostated glass cell filled with H_2SO_4 (0.5 M) or KOH (0.5 M) electrolytes. The reference electrode in H_2SO_4 was a Reversible Hydrogen Electrode (RHE), which was freshly prepared before each experiment as reported in literature [34]. In alkaline electrolyte a MMO, $Hg|HgO|OH^-_{(0.1\ M)}$ was used as reference electrode, which was weekly calibrated versus RHE, following the protocol described in literature [55]. A graphite rod was used as counter electrode, whereas a GC-disk (5 mm dia.) - Pt-ring RRDE was used as working - H_2O_2 sensor electrode. The electrochemical characterizations were performed on a film catalyst layer obtained by drop casting the catalyst ink on the GC disk of the RRDE, with a catalyst loading of 0.6 mg/cm^2. Before recording the electrochemical response, the carbon modified GC electrodes were activated by at least 50 voltammetric cycles performed at 200 mV s^{-1} or until a stable electrochemical voltammogram was obtained.

Mass-transport corrected kinetic current density was calculated according to Eq. (4).

$$j_{k,E} = \frac{j_{\lim} * j_E}{j_{\lim} - j_E} \tag{4}$$

where $j_{k,E}$ is the mass-transport corrected current density at a selected potential, $j_{\lim}$ is the limiting current density and j_E is the current density at the selected potential E. The number of exchanged electrons (n) was calculated according to Eq. (5):

$$n = \frac{4 i_D}{i_D + i_R/N} \tag{5}$$

where i_D (A) and i_R (A) are the absolute values of disk and ring currents, respectively, and N is the collection efficiency, ($N = 0.25$) determined by calibration with $Fe(CN)_6^{3-}$/ $Fe(CN)_6^{4-}$ redox couple. During RRDE experiments, the potential of the ring electrode was fixed at 1.50 and 1.56 V vs RHE in acid or in alkaline electrolyte, respectively. The percentage of hydrogen peroxide ($\%_{H_2O_2}$) was determined by

$$\%_{H_2O_2} = 100 \frac{2 i_R}{N * i_D + i_R} \tag{6}$$

To evaluate the Fe-N_x site density (SD), NO_2^- poisoning and electrochemical stripping were performed following the procedure described by Malko et al. [56]; this procedure allow to poison preferentially Fe-N_x in order to evaluate their density, measuring the charge of stripping during a CV measurement. The investigation of materials side density was performed on a thin layer of catalyst deposit on GC (RDE, PINE Research Ø = 5 mm) in a 0.5 M acetate buffer at pH 5.2. A loading of 0.2 mg cm^{-2} was chosen according to published procedure, the ink was let dry with the electrode in rotation at 130 rpm for about 20 min.

3. Results and discussion

3.1. Fe-N-C catalysts characterization

Figs. 2 and S2 report the TEM images of the resulting materials. EU900 exhibits a foam-like graphitic sheet with the apparent absence of any pore structure. The addition of $FeCl_3$ to the initial mixture leads to materials with more complex textural properties. In fact, Fe-EUs exhibit a spherical carbon structure and an intricated interconnection of hollow and open pores. In particular, moving from Fe-EU700 to Fe-EU900 the morphology becomes more ordered showing open alveoli-like structure with some nanotubes. This last feature is easily observed in Fe-U900 and it is a morphology typically obtained using metal NPs or PU as templating agents (Fig. 2f) [14,57]. The spherical morphology is mostly maintained even after the acid wash, which is aimed at removing the most part of inactive iron species [58]. Some scattered Fe-based particles covered with a less electron-dense carbon shell are nevertheless present. The carbon shell might exert a protection on iron particles enhancing the corrosion resistance and the stability of the catalysts also in very demanding pH condition.

A series of SEM images were acquired for Fe-EU800 before the acid treatment (Fig. S3). The carbon structure appears fragmented with aggregates differing by size and shape. Stacks of carbon nanolayer with a wrinkled surface are identified. As observed in literature, such roughness could be due to distorted graphene sheets comprised on the stacks [59]. The formation of big agglomerates and extended fragmentation is due to the pyrolysis of LDPE at high temperature [7], conversely the heat treatment of PU at

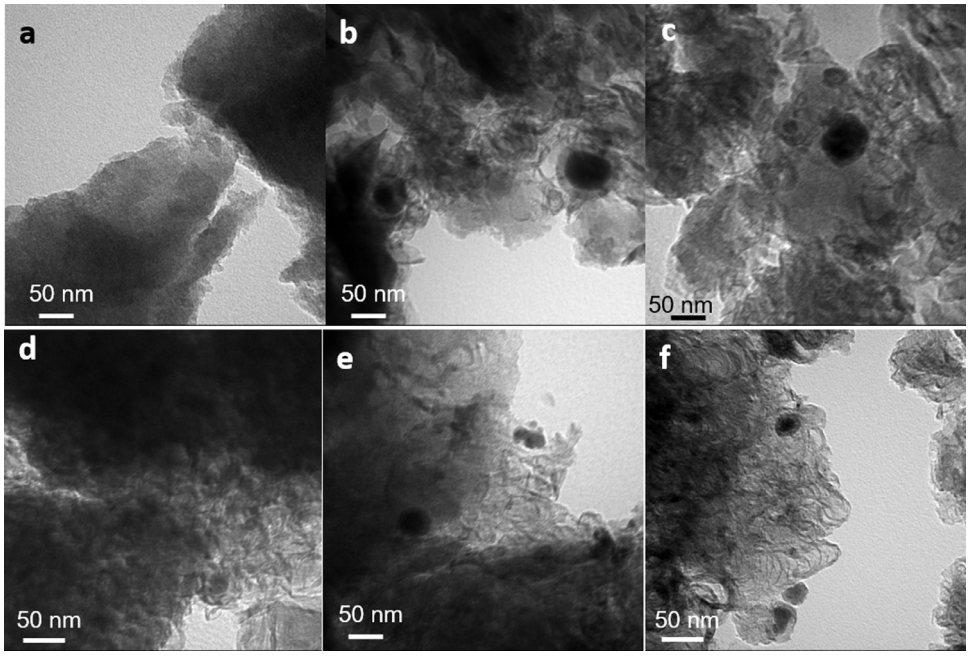

Fig. 2. TEM images of (a) EU900, (b) Fe-EU700, (c) Fe-EU800, (d) Fe-EU900, (e) Fe-EU1000 and (f) Fe-U900.

Table 1
Chemical and textural properties of the investigated Fe-N-C materials.

	C[a]	H[a] % wt	N[a]	S_{QSDFT} $m^2\ g^{-1}$	V_{TOT} $cm^3\ g^{-1}$	S_{μ} $m^2 g^{-1}$	V_{μ} $cm^3\ g^{-1}$	V_{meso} $cm^3\ g^{-1}$	V_{QSDFT}[b] $cm^3\ g^{-1}$	V_{macro} $cm^3\ g^{-1}$
EU900	80.84	1.05	6.40	41	0.061	24	0.008	0.027	0.034	0.027
Fe-EU700	85.67	0.71	1.75	323	0.261	234	0.074	0.119	0.193	0.068
Fe-EU800	82.94	0.92	2.03	293	0.275	230	0.074	0.106	0.180	0.095
Fe-EU900	91.78	0.3	0.91	195	0.266	151	0.030	0.150	0.184	0.082
Fe-EU1000	92.61	0.31	0.68	261	0.296	154	0.051	0.159	0.210	0.086
Fe-EU800B	77.54	0.95	2.38	243	0.315	201	0.076	0.102	0.178	0.137
Fe-U900	87.33	0.69	1.33	479	0.283	373	0.104	0.077	0.181	0.102

[a] Determined by CHN elemental analysis.
[b] (V_{μ} + V_{meso}) as determined by the QSDFT model.

temperature > 300°C leads to the rupture of PU foam cells into shards [60]. The EDX map element shows that iron is dispersed within the carbon support and even some Fe-based nanoparticles can be observed (Fig. S3c).

The pore size distribution and the surface area of the activated catalysts were determined from N_2 adsorption/desorption isotherms (Table 1). The Fe-N-C catalysts show an adsorption behavior in between type I(a) and II isotherms, where the steep uptake at low p/p^0 is due to the enhanced adsorbent-adsorptive interaction in narrow micropores (Fig. 3a,b) [61]. An H4 hysteresis loop is present in all the isotherms due to N_2 condensation inside micro and mesopores. The lower limit in the desorption branch is located at 0.45 p/p^0, which is the typical pressure for cavitation inside the pores and suggests the presence of ink-bottle shape of pores. Another interesting feature is the no-connection between adsorption and desorption branch; this usually happens because of the collapse of the structure. To reject this hypothesis, the analysis was repeated twice, finding a superimposable behavior of the final isotherms. A second and more reliable hypothesis is that N_2 adsorbed in the forward step remains confined inside the interconnected porosity, during the desorption step, because of the shape and size of pores [27]. EU900 showed a completely different isotherm, in fact the lack of an uptake at $p/p°$ close to zero is indicative of the absence of micropores, furthermore the hysteresis typical of micro and mesopore materials is absent (Fig. 3c). The analysis of pores was performed considering a cylindrical/sphere QSDFT adsorption branch model, which is more appropriated for microporous materials. Surface area and volume of micropores decrease with the increase of temperature, while in opposite direction evolves the volume of mesopores, which steps up with the temperature. Therefore, the total volume remains almost constant as result of compensation between the two types of porosity (Table 1). All the catalysts mainly present a microporous structure with micropores of 1.23 nm and small mesopores with diameter distribution centered at 3 and 7 nm (Fig. 3d,e). The presence of porosity is highly desirable in ORR catalysts since mesopores plays a pivotal role for the wetting of micropores where active sites are placed, whereas the macropores assure fast mass transport and accessibility of the active sites [41]. It is worth noting that Fe-U900, which was prepared by using only polyurethane, has the highest surface area (S_{QSDFT} = 479 $m^2\ g^{-1}$) mostly due to micropores. Therefore, it appears that the addition of polyethylene limits the formation of micropore and of a sponge like structure, which was evident in Fe-U900 TEM images. On the contrary EU900, which was prepared without iron, showed the lowest surface area (S_{QSDFT} = 41 $m^2\ g^{-1}$) and a very low content of micro- and mesopores (Fig. 3e). This highlights the pivotal role of iron in driving the textural properties of the final material.

Table 1 reports the CHN elemental analysis of all the synthetized samples. It is worth noting that the carbon content increases at the increase of the pyrolysis temperature, that is indicative of an increase of the graphitization degree with the temper-

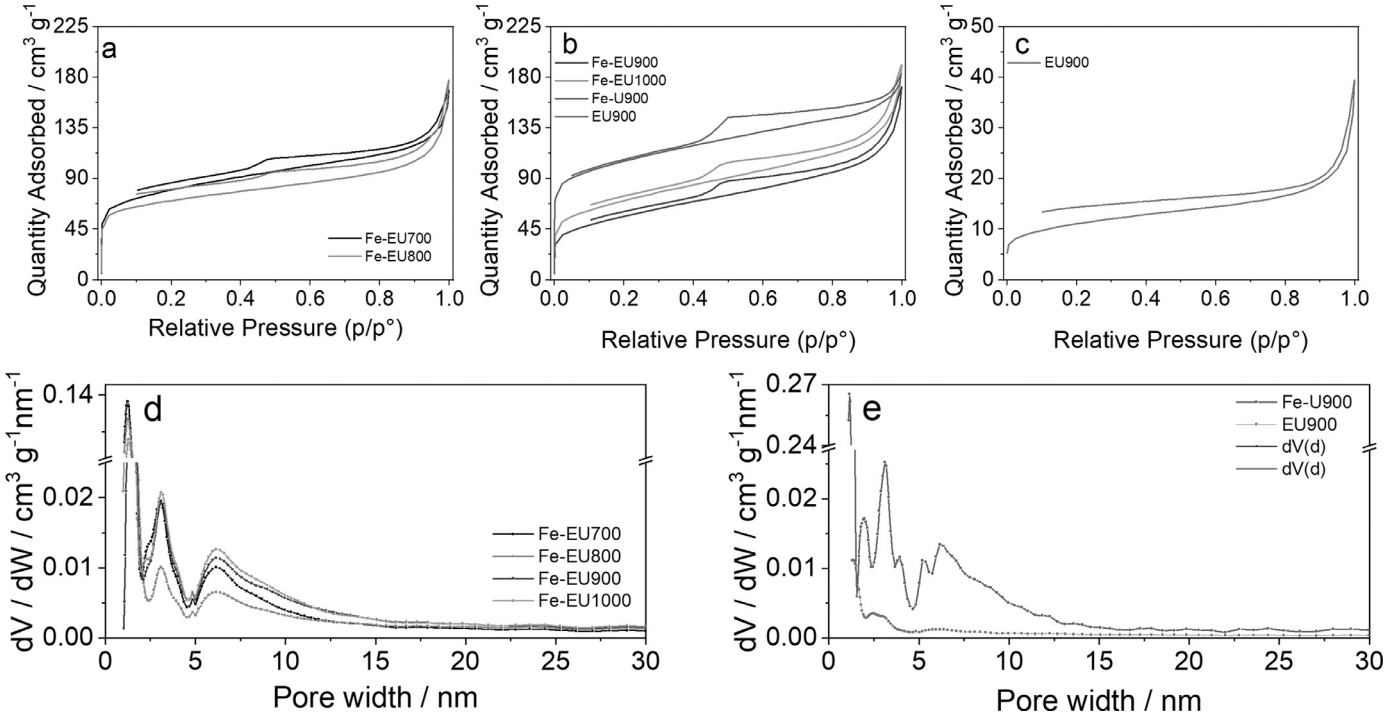

Fig. 3. (a–c) N_2 adsorption / desorption isotherm at 77 K, (c,d) and pore size distribution of all catalysts obtained by pyrolysis at different temperature and with or without PE or Fe.

ature. The employment of PU leads to the successful formation of N-C material, where the maximum value was observed in the iron free EU900 (6.40 %). The N% decreases when $FeCl_3$ is added to the polymer mixture and it decreases even more by enhancing the pyrolysis temperature (Table 1). In fact, beside the temperature, which exerts a well-known effect on the graphitization of carbon materials [25,62], iron is also known to catalyze the graphitization process [63]. Further insights about carbon graphitization are provided by XRD analysis, where a non-activated Fe-EU700 sample was characterized using a heating chamber in the temperature range 700–1000°C (Fig. 4a). At relatively low 2θ angle, it is visible the growth of a peak due to carbon that structures itself as graphite during heating. The 002 graphite reflection become sharper and more symmetric passing from 700 to 1000°C.

XRD analysis performed in the heating chamber is also helpful for understanding the evolution of different iron phases upon variation of second pyrolysis temperature. The measurement was performed on Fe-EU700 before acid washing (Fig. 4a). At ambient temperature, the starting sample exhibits reflections compatible with Fe_3C and α-Fe. The peaks at 46.4, 52.2, 54.2 and 71.4 °2θ are due to Pt strip used as chamber of the catalyst. The broad peak at 52 °2θ, underneath the iron reflections, describes the contribution of amorphous carbon. When the temperature is raised up to 700°C, the identified phases are: Fe_3C (orthorhombic) and α-Fe, while it is not certain the presence of magnetite (41 °2θ) and hematite (37.5 °2θ). The same phases are present also at 800°C, along with a small contribution attributed to γ-Fe. At 900°C, γ-Fe coexists with α-Fe, Fe_3C and magnetite. Raising the temperature at 1000°C, γ-Fe and Fe_3C are the only detectable phases. After reaching 1000°C, the sample is rapidly cooled down and the recognizable phases are: α-Fe, Fe_3C and γ-Fe, the latter exists in a metastable phase. The increasing or decreasing content of a crystalline phase (in a powder sample measured *in situ* during heating treatment) can be estimated taking into account the scale factor (SF) determined through Rietveld refinements (details of Rietveld refinements are reported in SI). The SF is proportional to integrated intensity of the Bragg reflections for each phase. Thus, it can be related with the content of each phase inside the volume of the irradiated sample. The increased SF for both α-Fe and γ-Fe, in Fig. 4c, reveals the increment of crystalline phase at the increasing of temperature. α-Fe is stable up to 900°C and γ-Fe can be detected starting from 800°C [64]. The heating at 1000°C followed by the rapid cooling at room temperature causes the increase of the α-Fe content and the presence of γ-Fe as a metastable phase. XRD analysis for Fe-EU700 was performed also on the samples after the activation treatment at 900°C under hydrogen flow (Fig. S4). The analysis was extended also to the other carbon samples and it is in plain view that the activation causes the increase of the graphitization degree in all the sample; as evident from the similar graphite reflection intensity (Fig. S4). The interpretation of XRD reflections of iron phases after the activation treatment is not trivial for Fe-EU800 and Fe-EU900, because of the presence of superimposed and not well-defined reflections (Figure S4), so that a rationale matching with the database was not possible. In sample Fe-EU700 the main diffraction peaks are related to Fe_3C and α-Fe. The XRD pattern lose definition moving from low to high second pyrolysis temperature, so much that the one at 1000°C did not show any iron discernible feature (data not reported). It seems that at higher temperature Fe-based particles are removed more easily as if they are ejected from the carbon matrix, which tries to reach a more ordered structure, resulting more exposed and therefore more easily removable by the acid wash.

Further insights of iron species were obtained by Mössbauer spectroscopy at room temperature (Fig. 4d). Fe-EU800 spectrum is dominated by an intense magnetic pattern between ≈-3.12 and ≈3.54 mm s^{-1}. A small broadening on the central lines can be referred to the presence of paramagnetic species while the weak absorptions at ≈-5.15 mm/s and ≈5.3 mm s^{-1} suggest the presence of accessory magnetically coupled components. Considering these evidences, the spectrum was fitted by the superimposition of five components: three sextets, one doublet and a singlet. Fe is mainly distributed over sextet 1 and doublet 1, representing the 68% and 19% of the total area respectively. Sextet 1 shows hyperfine param-

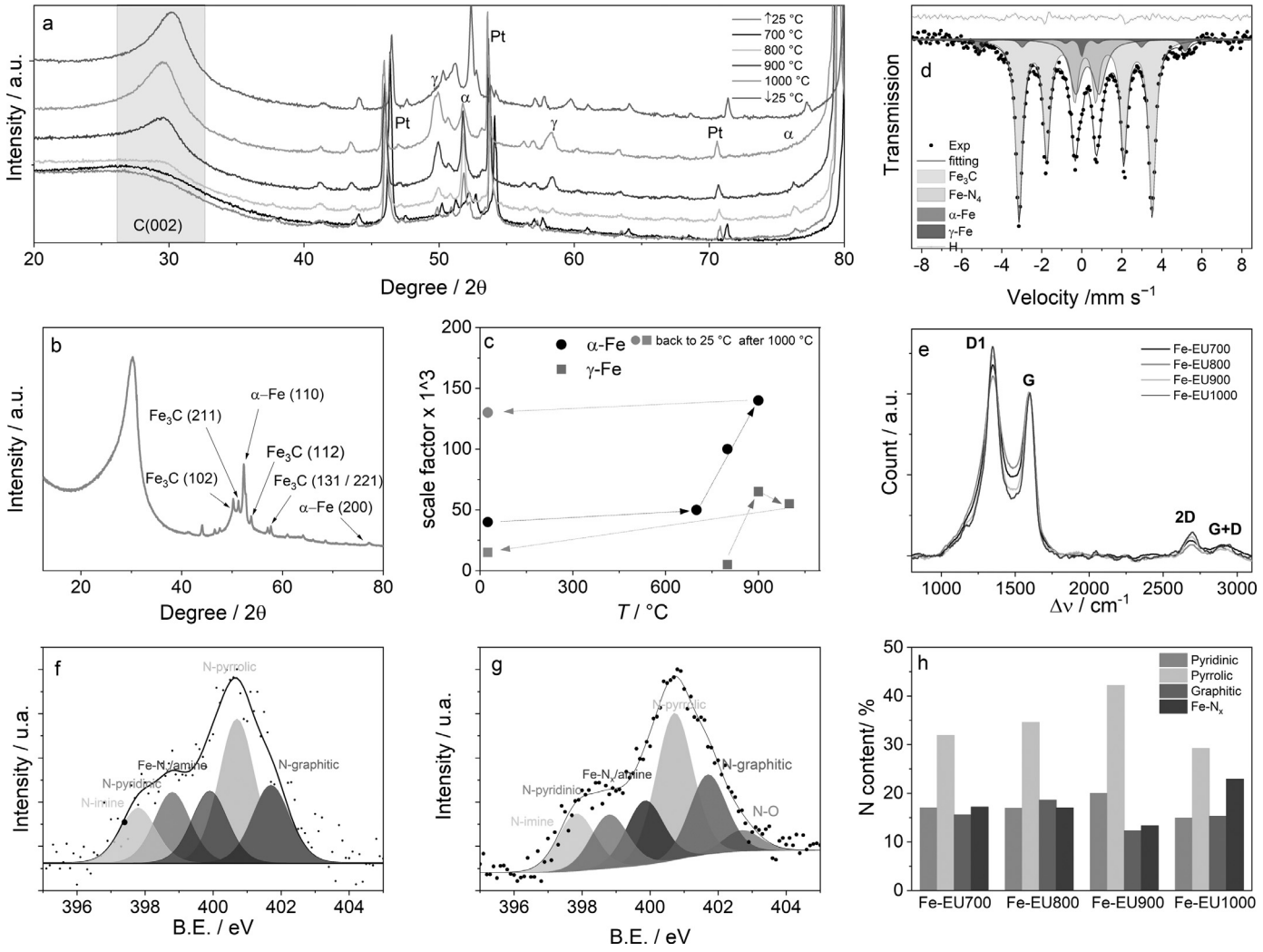

Fig. 4. (a) XRD characterization of Fe-EU700 using a heating chamber, (b) XRD reflection assignment, (c) scale factors, (d) Mössbauer spectra and Lorentzian fitting curves for Fe-EU800, (e) Raman spectra of several F-N-C materials, (f,g) High-resolution core-level XPS spectra of N 1s region and deconvolution into single chemical components for Fe-EU800 and Fe-U900, and (e) nitrogen functional group distribution by effect of temperature.

eters typical of intermetallic iron carbon compounds Fe_3C.[29] Doublet 1 can be reasonably attributed to Fe-N_4 sites but, due to its δ and Δ values, it cannot be unambiguously referred to a specific Fe oxidation and spin state. As a matter of fact, the δ can be assigned to low spin Fe(II) and/or Fe(III) in any spin state [65]. On the basis of the Δ, the discrimination can be restricted to low spin Fe (II) and/or high spin Fe(III) moieties, as reported in literature for Fe-N-C catalysts [65–67]. The presence of nanosized ferric oxides, in superparamagnetic (SPM) regime, can be excluded. Usually SPM nanoparticles in OOR catalyst show a doublet characterized by an higher δ values [68]. Concerning the minor contributions, the weak singlet centered at -0.01 mm s^{-1} can be ascribed to γ-Fe or superparamagnetic α-Fe, while sextet 2 to α-Fe (Table S1) [69,70].

Raman spectra were recorded for obtaining useful information about the graphitization degree in carbonaceous materials (Fig. 4d). The materials show two intense signals: the D1 band at ~1350 cm^{-1} and the G band at ~1595 cm^{-1}. The spectra were deconvoluted after baseline subtraction and normalization to the maximum of the G band. For the sake of an example, the deconvolution of Fe-EU800 is reported in Fig. S5a, were a combination of six gaussian-shaped bands (I, D4, D1, D3, G and D2) were used. The G band is attributed to ideal graphitic lattice, whereas the D1 band is due to disordered graphitic lattice (A_{1g}) and it has been suggested to arise from graphene layer carbon atoms in immediate vicinity of a lattice disturbance like heteroatoms. D2 band arises because of disordered graphene layers (E_{2g}) at the surface of a graphitic crystal. D3 is typical of amorphous carbon, whereas D4 and I, located close to each other, are due to disordered graphitic lattice (A_{1g}) and ionic impurities and they can be attributed to C-C and C=C stretching vibration of polyene-like structure [71]. In the range 2300 cm^{-1} - 3300 cm^{-1}, two more bands are present due to overtone and combination of graphitic lattice vibration modes. The 2D band centered at ~ 2690 cm^{-1} is attributed to the overtone of D1 and it indicates the formation of large domain size sp^2 carbon honeycomb structure [72]. The (G + D) combination has been assigned at 2933 cm^{-1} and it is typical for graphene oxide (GO) (Fig. 4e).

The intensity ratio between D and G band (I_D/I_G) is commonly used as indicator of the density of defects (Table S2), however I_{D1}/I_G ratio can be in some respects uncertain. It was proposed that the value R2 = D1/(G + D1 + D2), corresponding to the ratio of the areas of indicated band, is a more reliable parameter (Table 2) [73]. For poorly organized carbon materials R2 > 0.5, while a R2 < 0.5 is indicative of highly graphitized carbons. R2 value decreases from 0.66 to 0.43 passing from Fe-EU700 to Fe-EU1000. This demonstrates that at higher temperature the carbon structure

Table 2
Data obtained by deconvolution of Raman and XPS spetra.

	Raman			XPS spectroscopy									
	I_{D1}/I_G	R2[a]	A_{D3}	N_{TOT}[b] %$_{at}$	N_{TOT}[c] %$_{wt}$	N_{imine} % $_{at}$	$N_{pyridinic}$ % $_{at}$	$N_{Fe\text{-}Nx/amine}$ % $_{at}$	$N_{pyrrolic}$ % $_{at}$	$N_{graphitic}$ % $_{at}$	N-O % $_{at}$	Fe[b] %$_{at}$	Fe[c] %$_{wt}$
EU900	1.5	0.60	160.3	5.2	1.3	14.7	20	22.6	28.7	9.4	4.6	0.0	0.00
Fe-EU700	2.6	0.66	132.3	1.5	0.3	13.9	17	17.2	31.9	15.6	4.4	0.2	0.7
Fe-EU800	1.9	0.63	100.7	1.0	0.2	13.1	16.9	17	34.6	18.5	-	0.2	0.7
Fe-EU900	1.2	0.55	95.8	0.9	0.1	4.3	20	13.3	42.2	12.3	7.9	0.1	0.3
Fe-EU1000	0.8	0.43	72.1	1.4	0.4	17.7	14.9	22.9	29.2	15.3	-	0.2	1.0
Fe-EU800B	2.0	0.67	141.6	2.5	2.8	9.3	22.9	18.6	30.7	12.4	6.1	0.5	2.1
Fe-U900	1.4	0.53	90.0	1.2	0.2	13.5	12.7	15.2	34.8	18.9	4.9	0.1	0.3

[a] $R2 = (A_{D1})/(A_{D1} + A_{D2} + A_G)$.
[b] Atomic percentage
[c] weight percentage.

is more graphitized, resulting in a decrease of both the density of defects and of the D3 band associated to amorphous carbon, (Table 2).

Fig. S5b compares the Raman spectra of EU900, Fe-EU900 and Fe-U900. It is worth noting that the second order bands are missing in EU900, furthermore D1 and G bands are poorly resolved, D3 has the highest area (160.3) and an intense D4 band at 1250 cm^{-1} is present. All these evidences put in light the fundamental role of iron, even in low quantity, for improving the graphitization of the resulting carbon, whereas it is interesting to observe that the addition of PE to the precursor mix does not appears to sensitively affect the carbon organization (Fig. S5b).

The surface chemical composition of the catalysts after the activation treatment was investigated by XPS technique, which confirmed the presence of C, N, O and Fe (Fig. S6a, Table 2). In Fe-N-C samples, the nitrogen and iron content range between 0.9 - 1.5 % at. and 0.10 - 0.2 % at., respectively. Thorough acid wash generally ensures removal of iron-rich phase such as iron oxide nanoparticles with only atomically dispersed iron in coordination with nitrogen or graphite encapsulated iron NPs remaining. Both iron and nitrogen tend to decrease at the increase of temperature of pyrolysis and even if this effect is reasonable for nitrogen, since higher temperature of pyrolysis leads to an expulsion of nitrogen in the form of volatile species from the graphite lattice, the same cannot be said for iron. This effect was observed also by other groups even if no explanation were reported in literature. The decreasing of iron and nitrogen contents was also observed in a set of pyrolyses carried out at different time (0.5, 1 and 1.5 h) i.e. the nitrogen and iron content decrease in longer thermal treatments. In Table S2, CHN elemental analysis and ICP-MS iron determination before the acid leaching are reported. It is our belief that iron can forms volatile complexes such as iron pentacarbonyl and be expelled in the venting flow during the pyrolysis. However, this hypothesis was not confirmed by TGA-MS measurements, since no iron species were detected possibly because of a fast condensation before entering the MS sampler.

The N 1s XPS line was deconvoluted into six components centered at 397.8, 398.8, 399.9, 400.7, 401.7 and 402.7 eV, which correspond to imine, pyridinic, nitrogen coordinated to iron (Fe-N_x) or amine, pyrrolic, graphitic and oxidized N groups, respectively (Figs. 4f,g and S6b-e) [70,74–78]. Pyrrolic nitrogen is distinguished among all the other functional groups because it is the most abundant and its content increases with the increase of temperature till 900°C (Fig. 4f,g). Conversely, Fe-N_x functional group, which is supposed to be the most important active site for ORR, reaches its lowest value (13.3 %$_{at}$) in Fe-EU900. The formation of Fe-N_x sites is supported also by Mossbauer analysis which was performed on Fe-EU800 before acid leaching. The same comparison cannot be extended to the acid washed catalysts due to the very low amount of iron that would require very long experimental time (weeks) per sample and incorrect spectral areas, widths, and shape determination.

A completely different composition was found in Fe-EU1000, which presents an exceptional high nitrogen and iron contents with respect to the other catalysts (Table 2). It was found that Fe-N_x component is unexpectedly high (23 %), while the $N_{pyrrolic}$ is the lowest among all catalysts. It is known that nitrogen coordinated to iron is a highly stable group, therefore if Fe-N_x sites form upon reaching 1000°C, it would result more difficult their decomposition and the formation of volatile species. In the EU900 sample the peak at 399.9 eV was assigned to amine. No further insights are provided by the analysis of Fe 2p peak due to the low content of iron in all the samples (< 0.25 %$_{at}$).

3.2. Carbon catalysts from polymers mixed by a Brabender

Fe-EU800B was prepared by pyrolyzing a different PE/PU/Fe ratio with respect Fe-EU800, therefore a separate discussion is proposed. Fe-EU800B showed a type II isotherm, which is characteristic for non-porous or macroporous materials having a relatively small external surface (Fig. 5a). The sample exhibits a desorption branch, with a type-H3 open hysteresis loop, often observed in aggregates of plate-like particles, but also in macroporous material, where macropore are not completely filled with adsorbate at atmospheric pressure [79]. The comparison of the textural properties between the two samples Fe-EA800B and Fe-EA800, highlights a similar volume of micro and mesopore. The two sample differ for a lower micropore surface area in Fe-EU800B ($\Delta S_{QSDFT} = 50\ m^2\ g^{-1}$) (Table 1). Fig. 5b shows the XRD pattern for Fe-EU800B, which, despite the lower content of iron, shows the same iron phases then in Fe-EU800. The 002 reflection of graphite in Brabender-based sample is widened and not very intense, probably due to a low crystallinity of the material. This finds a confirmation by the Raman spectra of Fe-EA800B (Fig. 5c), which shows a high content of amorphous carbon as evident by the D3 band area (Table 2) and an R2 factor of 0.67. The elemental and XPS analysis determined a content of nitrogen of 2.38% and 2.5%, respectively, that evidence a homogeneous distribution of doping all over the sample (Tables 1 and 2). It is worth noting that Fe-EU800B presents a higher content of oxygen with respect to the samples prepared by using the solvent assisted approach, that is consistent with a less graphitized material. The N 1s peak was decomposed in 6 components, the pyrrolic and pyridinic ones being the most abundant (Fig. 5d).

3.3. ORR electrochemical tests

The ORR activity of Fe-N-C materials obtained at different pyrolysis temperature was evaluated in both acid (0.5 M H_2SO_4) and alkaline (0.5 M KOH) electrolytes at rotating ring disc electrode. The voltammetric response at a rotating electrode has generally a

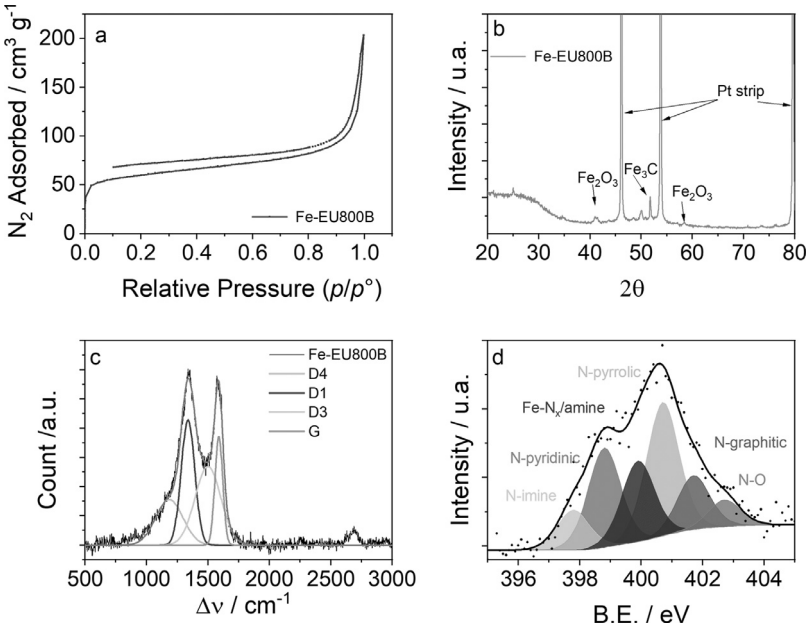

Fig. 5. Fe-EU800B characterization (a) Nitrogen adsorption/desorption isotherm, (b) XRD diffraction spectrum, (c) Raman spectrum and decomposition, (d) High-resolution core-level XPS spectrum of N 1s region and deconvolution into single chemical components.

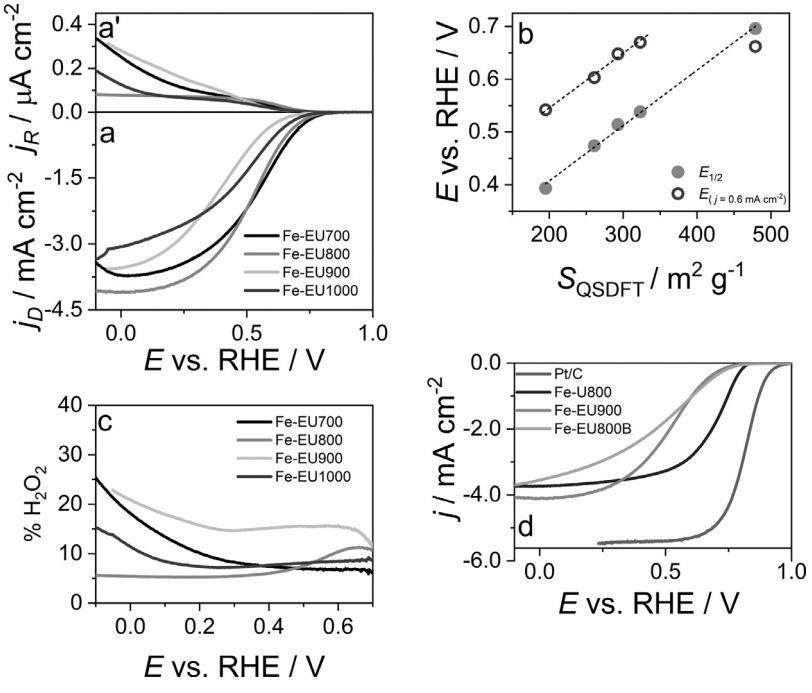

Fig. 6. Electrochemical data recorded at RRDE in O_2-saturated 0.5 M H_2SO_4. (a, a') LSV at RRDE at v = 5 mV s^{-1} and ω=1600 rpm, E_{app} (Ring) = 1.50 V vs. RHE; (b) correlation between $E_{1/2}$ or $E_{(j = 0.6\ mAcm^{-2})}$ and surface area determined from N_2 isotherm, c) H_2O_2 production during LSV in O_2-saturated solution; (d) comparison of electrochemical performances of commercial Pt/C, Fe-U900, Fe-EU800 and Fe-EU800B, at RDE in O_2-saturated solution (v = 5 mV s^{-1} and ω=1600 rpm).

sigmoid shape, which can be separated in three zone: *i*) a kinetic zone where the current depends by the kinetic of the reduction process (0.5 V < E < 0.9 V), *ii*) a mass transfer limited zone (E < 0.3 V), where the limiting current (i_{lim}) depends primarily on the rotation rate and on the active surface area, and *iii*) a mixed kinetic-mass transfer zone (0.3 V < E < 0.5 V), where the two effects determine the current profile. In the kinetic region, the half wave potentials ($E_{1/2}$) is the potential at $i_{lim}/2$, and it is a parameter that can be adopted to define the catalytic activity of the material. Fig. 6a compares the LSV at RDE of the investigated catalysts in 0.5 M H_2SO_4. It is in plain view that $E_{1/2}$ decreases in the order Fe-EU700 ≈ Fe-EU800 > Fe-EU1000 > Fe-EU900 that ascertain a higher catalytic activity for the catalysts prepared at a lower temperature of pyrolysis (Table 3). Fe-EU800 shows the highest i_{lim} which is indicative of a higher availability of active surface area (accessible active sites) compare to the other samples. It is worth noting that a good correlation between the $E_{1/2}$ and surface area determined by N_2-isotherm can be found, i.e. the higher the surface area, the higher the catalytic activity (Fig. 6b). Unfortunately, some of the half wave potentials used to compare the kinetic activity among the catalysts fall inside or close to mixed kinetic-mass-transfer zone. Therefore, to compare the real kinetic activity,

Table 3
Electrochemical data determined by RRDE measurements in 0.5 M H_2SO_4.

	$E_{1/2}$[a] V	$E_{(j\ =\ 0.6\ mAcm^{-2})}$[a] V	J_{lim}[b] mA cm^{-2}	n[c]	χ_{H2O2}[d] %	J_k[e] A g^{-1}
Fe-EU700	0.538	0.670	3.72	3.80	10	0.08
Fe-EU800	0.514	0.648	4.09	3.89	5	0.06
Fe-EU900	0.393	0.542	3.54	3.66	16	0.01
Fe-EU1000	0.474	0.603	3.07	3.85	7	0.02
Fe-EU800B	0.498	0.769	-3.52	3.81	11	0.09
Fe-U900	0.696	0.662	3.72	3.97	2	0.37

[a] Potential versus RHE.
[b] Current determined at 0.0 V normalized by geometrical surface area.
[c] Number of transferred electrons.
[d] H_2O_2 yield determined at 0.2 V.
[e] Kinetic current density determined at 0.8 V.

the potentials at 0.6 mA/cm² were considered, since at this value the current is less affected by mass transport. Also in this case, a good correlation between *E* and the surface area determined by N_2-isotherm can be found, provided the value for Fe-U800 is excluded from the plot. Both micro- and meso-pores appears to be important to increase the catalytic activity: the micropores because are supposed to host the catalytic sites while the mesopores assure the accessibility to micropores. As previously observed, Mossbauer and XPS spectroscopies failed to be conclusive in the determination and quantification of Fe-N_x sites. However, useful ways for confirming the formation of Fe-N_x sites is the selective poisoning of metal sites using different anion or molecule like NO_2^- [56]. The electrochemical method proposed by Malko et al. is based on the reversible and selective interaction of Fe-N_x sites with probe molecule NO_2^-, which in acid pH is converted to nitrosyl binding to Fe center. As shown in Fig. S7a, when the catalyst layer is poisoned, there is an excess of cathodic charge (yellow area), which disappears on subsequent voltammetric scan. The stripping charge, Q_{strip}, is calculated from the area of the stripping peak considering the scan rate and the mass of loaded catalysts and permits to determine the gravimetric site density according to the formula:

$$MSD\ \left[mol\ sites\ g^{-1}\right] = \frac{Q_{strip}\left[C\ g^{-1}\right]}{n_{stip}F[C\ mol^{-1}]} \quad (7)$$

where n_{stip} is the number of electrons associated with the reduction of one adsorbed nitrosyl per site to NH_3. Fig. S7b shows the ORR performance of the Fe-PU800 catalyst as a function of poisoning. The catalyst performance is significantly reduced by the presence of an adsorbed nitrite intermediate, leading to a 45 mV shift in performance at 0.6 V (RHE). Thus, activity of the catalyst is sensitively reduced with respect to its unpoisoned state. Following the stripping process, the ORR performance is almost completely recovered (Fig. S7b). For Fe-EU800 catalyst the determined MSD value was $5.45 \cdot 10^{18}$ sites g^{-1}, which is not far from values obtained from other PGM free benchmark catalysts proposed in literature [81] and that undoubtedly confirms the formation and presence of iron single sites. Interestingly, even after poisoning, the catalysts is still partially active versus ORR meaning that also other catalytic sites are present and are responsible for the reduction process as the pyridinic, pyrrolic and nitrogen substitutional functional groups [39,76].

The overall peroxide/water yield can be determined by a comparison between the ring and disk currents of RRDE experiments, according to Eqs. (5) and (6). In a RRDE experiment, O_2 is reduced at the GC disk electrode, which is coated with the Fe-N-C catalyst, by sweeping the potential from high to lower values. The rotation movement of the electrode forces the reaction products to move towards the ring electrode, which is polarized at a fix potential at which H_2O_2 quickly oxidizes back to O_2. Therefore, if H_2O_2 is produced at the disk electrode and if it is not trapped inside the catalyst layer, the ring electrode works as a H_2O_2 detector provided no other secondary reactions occur. The disk and the ring electrode are linked by the collection efficiency (N), which depends on the RRDE geometry and equals 0.25 in our case. Therefore, if O_2 is exclusively reduced to H_2O, the ring current tends to zero, on the contrary if H_2O_2 is the exclusive product, the ring current will be 25% of the disk current. Generally, the experimental results fall in between the two limiting cases, aka a mix of the two mechanism is always present. Therefore, the RRDE analysis is by itself not always the direct expression of a particular mechanism, especially at low peroxide yield where the mechanism can follow both a tetraelectronic mechanism or a two electron electrochemical reduction + a two electron chemical reduction (2+2), which are two different mechanisms undistinguishable using RRDE. Among Fe-EUx catalysts, the H_2O_2 yields at 0.2 V ranges between 5 and 16 %, where Fe-EU800 is the one producing the lowest amount (Table 3). Apparently, χ_{H2O2} is lower in those catalysts showing higher surface area, and this can be tentatively related to the better accessibility to the N_x-Fe active sites positioned in micropores (Fig. 6c). A further comment needs to be made about the limiting current density of the examined catalysts. In fact, even though the RRDE findings are consistent with a low H_2O_2 yield, the limiting current density are much lower with respect to that expected for a tetraelectronic reduction of oxygen, and this is even more evident when Fe-N-C catalysts are compared to the Pt/C standard (Fig. 6d). Such a difference could be related to the relatively high loadings used for the RDE analysis (0.6 mg/cm²) resulting in relatively thick catalyst layers which might hinder the release of the H_2O_2 fraction [80].

Fig. 6d compares the LSV at RDE of the best performing catalyst Fe-EU800 and of Fe-EU800B, which was prepared by mixing the components with a Brabender plastograph. It is worth to be observed that the kinetic zone is almost superimposable while in the diffusion area and mixed kinetic-diffusion zone Fe-EU800B shows a kinetic current and a limiting current much lower than Fe-EU800. This may be explained by the presence of many Fe surface sites in the Fe-EU800B micropores, which failed to be accessible, and hence effective under electrochemical conditions. In fact even though Fe-EU800B has higher N and Fe contents and therefore a higher content of active sites than Fe-EU800 (Table 2), it has a lower mesopore surface area and volume (Table 1) and therefore mass transport to active sites is hindered [81]. This hypothesis finds a confirmation considering Fe-U900, which was prepared without PE and that was characterized by a microporous and mesopore surface superior with respect to both Fe-EU800B and Fe-EU800. In fact, Fe-U900 showed the best $E_{1/2} = 0.696$ V and kinetic current (j_k = of 0.37 A g^{-1}) at 0.8 V (Table 3). Furthermore, oxygen and/or nitrogen-based functional groups are known to play a complementary role during ORR [25]. In fact, oxygen functional groups decrease the electrochemical activity of catalysts due to possible production of hydrogen peroxide as intermediate [82]. Therefore,

the high content of oxygen functional groups in Fe-EU800B along with less accessible active site can hinder the ORR performance of the catalyst. The Pt/C benchmark, was also reported here for the sake of comparison (Fig. 6d), highlighting that Fe-EU800 is still far from being competitive with Pt/C benchmark in term of catalytic activity versus ORR but PE and PU are raw materials far more disposable and economically competitive than platinum. Furthermore, further activity improvements can be reached by improving the textural properties and the density of active sited by introducing post pyrolysis activation treatments [23]. Even thou the aim of the paper was to consider the conversion of a mixed waste polymer in Fe-N-C catalyst, one last comment must be made on Fe-U900 which showed the best ORR activity (Table 3). Fe-U900 has a lower content of Fe-N_x sites with respect to Fe-EU900 but a higher surface area especially in term of mesopores (Tables 1 and 2). The superior activity may be explained considering that Fe-U900 contains better exposed and accessible Fe-N_x sites than Fe-EU900. Primbs et al. carried out a systematic work on four of today's most active benchmark Fe-N-C catalysts and demonstrated that microporous catalyst showed large site density (SD) values paired with low turn over frequency (TOF), while mesoporous catalysts displayed the opposite. Therefore, it is reasonable to assert that Fe-U900 is characterized by a low SD but by a high TOF as it was proposed in the above mentioned paper [81]. The optimization of Fe-U900 catalysts and the determination of SD and TOF is not the aim of this paper but it is part of an ongoing research on Fe-N-C catalysts derived from waste thermoset polymers.

The electrochemical characterization was extended also to alkaline electrolyte. The current potential curves at RRDE of Fe-EUx in an O_2 saturated 0.5 M KOH electrolyte are shown in Fig. S8a. The LSVs are composed of two reduction steps of almost the same height, and the current features are superimposable for all four catalysts, thus confirming comparable electrochemical behaviors for all samples, notwithstanding the pyrolysis temperature. Therefore, a catalytic effect is present but the O_2 reduction occurs approximately at the same potential for all catalysts, for example the $E_{1/2}$ values of the first step range between 0.705 to 0.722 V vs. RHE (Table S3). The ring current of RRDE electrode increases and then assumes a constant value nearby the first O_2 reduction step, whereas at the second O_2 reduction step the ring current decreases reaching an almost steady value (Fig. S8a'). The number of electrons determined according to Eq. (5) agrees with the preferential production of H_2O_2 in the first step and H_2O in the second one. Therefore, it can be assumed that in alkaline environment the O_2 is at first reduced to H_2O_2, and then further reduced in the second step, at far more negative potentials, to H_2O. The selectivity toward H_2O_2 production was found to be almost 60% for all the samples when the potential was limited to the first reduction step (Fig. S8b).

The different H_2O_2 selectivity passing from acid to alkaline electrolyte clearly indicates that ORR occurs on different active site depending on the pH. Fe-N_x sites promote O_2 reduction to both H_2O_2 and water, but in acid electrolytes the peroxide desorbs rapidly from the Fe-N_x active sites so that cocatalysts such as Fe encapsulated in few carbon layers or Fe_3C are necessary to complete the tetra-electron mechanism [75]. In alkaline media Fe-N_x site prompts the O_2 adsorption and $2e^-$ reduction to peroxide intermediate, which is subsequently reduced on the same active sites. Another important active site is the pyrrolic functional group, which causes partial reduction of oxygen to hydrogen peroxide. It is not the aim of this paper to define the reduction mechanism at different pH, however, it is in plain view that different active sites are at play during ORR and depending on the pH the active sites are activated or disactivated because of protonation/deprotonation [25] or even hydroxylation [83] of the active site or of the atoms nearby the adsorption site.

4. Conclusion

Fe-N-C catalysts were successfully synthetized from the two-stage pyrolysis of a mix of thermoset (PU) and thermoplastic (PE) polymers, mimicking an undifferentiated polymer waste and $FeCl_3$ as iron source. Before pyrolysis the precursors were mixed following a solvent assisted or a solvent free procedure. The presence of $FeCl_3$ was fundamental for increasing both the surface area, which ranges between 195 and 479 $m^2\ g^{-1}$, and the graphitization degree of the materials. It was found that the second pyrolysis temperature affects the chemical and textural properties of the Fe-N-C materials, such as the surface area, the graphitization degree, the nitrogen and iron content and as a consequence the catalytic activity of the materials. The combination of XRD, XPS, Mossbauer spectroscopies and NO-reductive stripping method allowed the identification of Fe-N_x, Fe_3C and metallic iron nanoparticles encapsulated in graphite layers.

The catalytic properties of Fe-N-C materials towards the ORR were investigated in both acid and alkaline solution. At acid pH there is a clear correlation between the catalytic activity expressed as $E_{1/2}$ with the surface area, i.e. the higher the surface area, the higher the catalytic activity. This effect was explained considering that high surface area allows a higher number of accessible active sites. Furthermore, a preferential 4 electron reduction to H_2O was found on all materials especially in those possessing higher surface area (H_2O_2 yield < 5 %). At high pH, the Fe-N-C materials show high catalytic activity ($E_{1/2}$ = 705-722 V), but it is difficult to discriminate substantial differences among different catalysts. Furthermore, it was found an inversed selectivity with respect the acid electrolyte, with a H_2O_2 yield exceeding 60 %. The different catalytic activity and selectivity towards ORR clearly depends on the different active sites (Fe-N_x, Fe_3C, Fe@C, N-pyrrolic, N-pyridinic, etc), which can catalyse the ORR and that can be activated or deactivated depending on the pH

Credit author statement

Giorgia Daniel synthetized the catalysts and performed the electrochemical characterization and data analysis

Tomasz Kosmala performed XPS and Raman measurements

Maria Chiara Dalconi, performed XRD analysis

Luca Nodari, performed Mossbauer measurements

Denis Badocco, performed ICP analysis

Paolo Pastore, performed ICP analysis

Alessandra Lorenzetti, synthetized PU foam and carried out Brabender molding of the polymers

Gaetano Granozzi, provided paper revision

Christian Durante, conceived the original idea, wrote the manuscript, supervised the project.

Declaration of Competing Interest

The authors declare that they have no known competing financial interests or personal relationships that could have appeared to influence the work reported in this paper.

Acknowledgment

The research leading to these results has received funding from the Fuel Cells and Hydrogen 2 Joint Undertaking under grant agreement No 779366, CRESCENDO. This Joint Undertaking receives support from the European Union's Horizon 2020 research and innovation programme, Hydrogen Europe and Hydrogen Europe Research.

Supplementary materials

Supplementary material associated with this article can be found, in the online version, at doi:10.1016/j.electacta.2020.137200.

References

[1] G.M. Lewis, C.A. Buchanan, K.D. Jhaveri, J.L. Sullivan, J.C. Kelly, S. Das, A.I. Taub, G.A. Keoleian, Green principles for vehicle lightweighting, Environ. Sci. Technol. 53 (2019) 4063–4077, doi:10.1021/acs.est.8b05897.

[2] M. Noroozi, M. Panahi-Sarmad, M. Abrisham, A. Amirkiai, N. Asghari, H. Golbaten-Mofrad, N. Karimpour-Motlagh, V. Goodarzi, A.R. Bahramian, B. Zahiri, Nanostructure of aerogels and their applications in thermal energy insulation, ACS Appl. Energy Mater. 2 (2019) 5319–5349, doi:10.1021/acsaem.9b01157.

[3] X. Zhao, K. Cornish, Y. Vodovotz, Narrowing the gap for bioplastic use in food packaging: an update, Environ. Sci. Technol. 54 (2020) 4712–4732, doi:10.1021/acs.est.9b03755.

[4] B.Liu Kenry, Recent advances in biodegradable conducting polymers and their biomedical applications, Biomacromolecules 19 (2018) 1783–1803, doi:10.1021/acs.biomac.8b00275.

[5] J. Scheirs, Polymer Recycling: Science, Technology and Applications, 1st ed., John Wiley & Sons, Chichester, 1998 http://link.springer.com/10.1007/978-94-011-0623-8_13.

[6] J. Gong, J. Liu, X. Chen, Z. Jiang, X. Wen, E. Mijowska, T. Tang, Striking influence of NiO catalyst diameter on the carbonization of polypropylene into carbon nanomaterials and their high performance in the adsorption of oils, RSC Adv. 4 (2014) 33806–33814, doi:10.1039/C4RA05016A.

[7] M. Soganciogl u, E. Yel, G. Ahmetli, Pyrolysis of waste high density polyethylene (HDPE) and low density polyethylene (LDPE) plastics and production of epoxy composites with their pyrolysis chars, J. Clean. Prod. 165 (2017) 369–381, doi:10.1016/j.jclepro.2017.07.157.

[8] A.Y. Snegirev, M.K. Handawy, V.V. Stepanov, V.A. Talalov, Pyrolysis and combustion of polymer mixtures: exploring additivity of the heat release rate, Polym. Degrad. Stab. 161 (2019) 245–259, doi:10.1016/j.polymdegradstab.2019.01.037.

[9] C. You, S. Liao, X. Qiao, X. Zeng, F. Liu, R. Zheng, H. Song, J. Zeng, Y. Li, Conversion of polystyrene foam to a high-performance doped carbon catalyst with ultrahigh surface area and hierarchical porous structures for oxygen reduction, J. Mater. Chem. A. 2 (2014) 12240–12246, doi:10.1039/C4TA02225D.

[10] J. Duan, H. Fan, W. Shen, Nitrogen-doped carbon materials prepared from polyurethane foams, ChemistrySelect 1 (2016) 3204–3207, doi:10.1002/slct.201600403.

[11] C. Ge, J. Song, Z. Qin, J. Wang, W. Fan, Polyurethane foam-based ultramicroporous carbons for CO_2 capture, ACS Appl. Mater. Interfaces. 8 (2016) 18849–18859, doi:10.1021/acsami.6b04771.

[12] A. Bazargan, G. McKay, A review - Synthesis of carbon nanotubes from plastic wastes, Chem. Eng. J. 195–196 (2012) 377–391, doi:10.1016/j.cej.2012.03.077.

[13] J. Gong, J. Liu, Z. Jiang, X. Chen, X. Wen, E. Mijowska, T. Tang, Converting mixed plastics into mesoporous hollow carbon spheres with controllable diameter, Appl. Catal. B Environ. 152–153 (2014) 289–299, doi:10.1016/j.apcatb.2014.01.051.

[14] J. Deng, Y. You, V. Sahajwalla, R.K. Joshi, Transforming waste into carbon-based nanomaterials, Carbon 96 (2016) 105–115, doi:10.1016/j.carbon.2015.09.033.

[15] Y. Wen, K. Kierzek, X. Chen, J. Gong, J. Liu, R. Niu, E. Mijowska, T. Tang, Mass production of hierarchically porous carbon nanosheets by carbonizing “real-world” mixed waste plastics toward excellent-performance supercapacitors, Waste Manag 87 (2019) 691–700, doi:10.1016/j.wasman.2019.03.006.

[16] K. Liang, L. Liu, W. Wang, Y. Yu, Y. Wang, L. Zhang, C. Ma, A. Chen, Conversion of waste plastic into ordered mesoporous carbon for electrochemical applications, J. Mater. Res. 34 (2019) 941–949, doi:10.1557/jmr.2018.493.

[17] Y.-M. Lian, W. Utetiwabo, Y. Zhou, Z.-H. Huang, L. Zhou, F. Muhammad, R.-J. Chen, W. Yang, From upcycled waste polyethylene plastic to graphene/mesoporous carbon for high-voltage supercapacitors, J. Colloid Interface Sci. 557 (2019) 55–64, doi:10.1016/j.jcis.2019.09.003.

[18] B. Li, C. Zhao, J. Liu, Q. Zhang, Electrosynthesis of hydrogen peroxide synergistically catalyzed by atomic Co–N_x–C sites and oxygen functional groups in noble-metal-free electrocatalysts, Adv. Mater. 31 (2019) 1808173, doi:10.1002/adma.201808173.

[19] J.G.S. Moo, A. Veksha, W.-D. Oh, A. Giannis, W.D.C. Udayanga, S.-X. Lin, L. Ge, G. Lisak, Plastic derived carbon nanotubes for electrocatalytic oxygen reduction reaction: Effects of plastic feedstock and synthesis temperature, Electrochem. Commun. 101 (2019) 11–18, doi:10.1016/j.elecom.2019.02.014.

[20] J. Gong, X. Chen, T. Tang, Recent progress in controlled carbonization of (waste) polymers, Prog. Polym. Sci. 94 (2019) 1–32, doi:10.1016/j.progpolymsci.2019.04.001.

[21] Y. Wen, J. Liu, J. Song, J. Gong, H. Chen, T. Tang, Conversion of polystyrene into porous carbon sheets and hollow carbon shells over different magnesium oxide templates for efficient removal of methylene blue, RSC Adv. 5 (2015) 105047–105056, doi:10.1039/C5RA18505J.

[22] Y. Hu, J. Yang, J. Tian, L. Jia, J.S. Yu, Green and size-controllable synthesis of photoluminescent carbon nanoparticles from waste plastic bags, RSC Adv. 4 (2014) 47169–47176, doi:10.1039/c4ra08306g.

[23] G. Daniel, E. Foltran, R. Brandiele, L. Nodari, R. Pilot, E. Menna, G.A. Rizzi, A.A. Isse, C. Durante, A. Gennaro, Platinum-free electrocatalysts for oxygen reduction reaction: Fe-Nx modified mesoporous carbon prepared from biosources, J. Power Sources 402 (2018) 434–446, doi:10.1016/j.jpowsour.2018.09.060.

[24] V. Perazzolo, C. Durante, A. Gennaro, Nitrogen and sulfur doped mesoporous carbon cathodes for water treatment, J. Electroanal. Chem. 782 (2016) 264–269, doi:10.1016/j.jelechem.2016.10.037.

[25] V. Perazzolo, C. Durante, R. Pilot, A. Paduano, J. Zheng, G.A. Rizzi, A. Martucci, G. Granozzi, A. Gennaro, Nitrogen and sulfur doped mesoporous carbon as metal-free electrocatalysts for the in situ production of hydrogen peroxide, Carbon 95 (2015) 949–963, doi:10.1016/j.carbon.2015.09.002.

[26] G. Daniel, Y. Zhang, S. Lanzalaco, F. Brombin, T. Kosmala, G. Granozzi, A. Wang, E. Brillas, I. Sirés, C. Durante, Chitosan-derived nitrogen-doped carbon electrocatalyst for a sustainable upgrade of oxygen reduction to hydrogen peroxide in UV-assisted electro-fenton water treatment, ACS Sustain. Chem. Eng. (2020), doi:10.1021/acssuschemeng.0c04294.

[27] E. Trevisanello, F. De Bon, G. Daniel, F. Lorandi, C. Durante, A.A. Isse, A. Gennaro, Electrochemically mediated atom transfer radical polymerization of acrylonitrile and poly(acrylonitrile-b-butyl acrylate) copolymer as a precursor for N-doped mesoporous carbons, Electrochim. Acta 285 (2018) 344–354, doi:10.1016/j.electacta.2018.07.209.

[28] V. Perazzolo, G. Daniel, R. Brandiele, L. Picelli, G.A. Rizzi, A.A. Isse, C. Durante, PEO-b-PS Block Copolymer Templated Mesoporous Carbons, A comparative study of nitrogen and sulfur doping in the oxygen reduction reaction to hydrogen peroxide, Chem. A Eur. J. (2020), doi:10.1002/chem.202003355.

[29] R. Ciriminna, L. Albanese, F. Meneguzzo, M. Pagliaro, Hydrogen Peroxide, A key chemical for today’s sustainable development, ChemSusChem 9 (2016) 3374–3381, doi:10.1002/cssc.201600895.

[30] M. Shao, Q. Chang, J.-P. Dodelet, R. Chenitz, Recent advances in electrocatalysts for oxygen reduction reaction, Chem. Rev. 116 (2016) 3594–3657, doi:10.1021/acs.chemrev.5b00462.

[31] R. Brandiele, M. Zerbetto, M.C. Dalconi, G.A. Rizzi, A.A. Isse, C. Durante, A. Gennaro, Mesoporous carbon with different density of thiophenic-like functional groups and their effect on oxygen reduction, ChemSusChem 12 (2019) 4229–4239, doi:10.1002/cssc.201901568.

[32] V. Perazzolo, R. Brandiele, C. Durante, M. Zerbetto, V. Causin, G.A. Rizzi, I. Cerri, G. Granozzi, A. Gennaro, Density functional theory (DFT) and experimental evidences of metal–support interaction in platinum nanoparticles supported on nitrogen- and sulfur-doped mesoporous carbons: synthesis, activity, and stability, ACS Catal 8 (2018) 1122–1137, doi:10.1021/acscatal.7b03942.

[33] R. Brandiele, C. Durante, M. Zerbetto, N. Vicentini, T. Kosmala, D. Badocco, P. Pastore, G.A. Rizzi, A.A. Isse, A. Gennaro, Probing the correlation between Pt-support interaction and oxygen reduction reaction activity in mesoporous carbon materials modified with Pt-N active sites, Electrochim. Acta 277 (2018) 287–300, doi:10.1016/j.electacta.2018.04.182.

[34] R. Brandiele, C. Durante, E. Grądzka, G.A. Rizzi, J. Zheng, D. Badocco, P. Centomo, P. Pastore, G. Granozzi, A. Gennaro, One step forward to a scalable synthesis of platinum–yttrium alloy nanoparticles on mesoporous carbon for the oxygen reduction reaction, J. Mater. Chem. A. 4 (2016) 12232–12240, doi:10.1039/C6TA04498K.

[35] Y.-J. Wang, N. Zhao, B. Fang, H. Li, X.T. Bi, H. Wang, Carbon-supported Pt-based alloy electrocatalysts for the oxygen reduction reaction in polymer electrolyte membrane fuel cells: particle size, shape, and composition manipulation and their impact to activity, Chem. Rev. 115 (2015) 3433–3467, doi:10.1021/cr500519c.

[36] X. Wang, Z. Li, Y. Qu, T. Yuan, W. Wang, Y. Wu, Y. Li, Review of metal catalysts for oxygen reduction reaction: from nanoscale engineering to atomic design, Chem 5 (2019) 1486–1511, doi:10.1016/j.chempr.2019.03.002.

[37] L. Bloxham, S. Brown, L. Cole, A. Cowley, M. Fujita, N. Girardot, J. Jiang, R. Raithatha, M. Ryan, E. Shao, F. Xiaoyan, JM - PGM Market Report, 2020.

[38] A. Facchin, T. Kosmala, A. Gennaro, C. Durante, Electrochemical scanning tunneling microscopy investigations of fen_4 -based macrocyclic molecules adsorbed on Au(111) and their implications in the oxygen reduction reaction, ChemElectroChem 7 (2020) 1431–1437, doi:10.1002/celc.202000137.

[39] U. Tylus, Q. Jia, N. Strickland, A. Ramaswamy, A. Serov, P.B. Atanassov, S. Mukerjee, Elucidating oxygen reduction active sites in pyrolyzed metal-nitrogen coordinated non-precious electrocatalyst systems, J. Phys. Chem. C. 118 (2014) 8999–9008, doi:10.1021/jp500781v.

[40] X. Zhang, X. Han, Z. Jiang, J. Xu, L. Chen, Y. Xue, A. Nie, Z. Xie, Q. Kuang, L. Zheng, Atomically dispersed hierarchically ordered porous Fe–N–C electrocatalyst for high performance electrocatalytic oxygen reduction in Zn-Air battery, Nano Energy 71 (2020) 104547–104556, doi:10.1016/j.nanoen.2020.104547.

[41] S.H. Lee, J. Kim, D.Y. Chung, J.M. Yoo, H.S. Lee, M.J. Kim, B.S. Mun, S.G. Kwon, Y.E. Sung, T. Hyeon, Design principle of Fe-N-C electrocatalysts: how to optimize multimodal porous structures? J. Am. Chem. Soc. 141 (2019) 2035–2045, doi:10.1021/jacs.8b11129.

[42] F. Jaouen, D. Jones, N. Coutard, V. Artero, P. Strasser, A. Kucernak, Toward platinum group metal-free catalysts for hydrogen/air proton-exchange membrane fuel cells, Johnson Matthey Technol. Rev. 62 (2018) 231–255, doi:10.1595/205651318X696828.

[43] X. Chen, N. Wang, K. Shen, Y. Xie, Y. Tan, Y. Li, MOF-derived isolated Fe atoms implanted in N-Doped 3D hierarchical carbon as an efficient ORR electrocatalyst in both alkaline and acidic media, ACS Appl. Mater. Interfaces 11 (2019) 25976–25985, doi:10.1021/acsami.9b07436.

[44] F. Xiao, G.-L. Xu, C.-J. Sun, M. Xu, W. Wen, Q. Wang, M. Gu, S. Zhu, Y. Li, Z. Wei, X. Pan, J. Wang, K. Amine, M. Shao, Nitrogen-coordinated single iron atom catalysts derived from metal organic frameworks for oxygen reduction reaction, Nano Energy 61 (2019) 60–68, doi:10.1016/j.nanoen.2019.04.033.

[45] A. Morozan, F. Jaouen, Metal organic frameworks for electrochemical applications, Energy Environ. Sci. 5 (2012) 9269–9290, doi:10.1039/c2ee22989g.
[46] D. Wang, J. Hu, J. Yang, K. Xiao, S. Liang, J. Xu, B. Liu, H. Hou, Fe and N co-doped carbon derived from melamine resin capsuled biomass as efficient oxygen reduction catalyst for air-cathode microbial fuel cells, Int. J. Hydrogen Energy 45 (2020) 3163–3175, doi:10.1016/j.ijhydene.2019.11.201.
[47] J.-S.M. Lee, S. Sarawutanukul, M. Sawangphruk, S. Horike, Porous Fe–N–C catalysts for rechargeable zinc–air batteries from an iron-imidazolate coordination polymer, ACS Sustain. Chem. Eng. 7 (2019) 4030–4036, doi:10.1021/acssuschemeng.8b05403.
[48] B. Feng, X. Wu, Y. Niu, W. Li, Y. Yao, W. Hu, C.M. Li, Hierarchically porous Fe/N–C hollow spheres derived from melamine/Fe-incorporated polydopamine for efficient oxygen reduction reaction electrocatalysis, Sustain. Energy Fuels. 3 (2019) 3455–3461, doi:10.1039/C9SE00686A.
[49] C. Li, F. Sun, Y. Lin, Refining cocoon to prepare (N, S, and Fe) ternary-doped porous carbon aerogel as efficient catalyst for the oxygen reduction reaction in alkaline medium, J. Power Sources 384 (2018) 48–57, doi:10.1016/j.jpowsour.2018.01.020.
[50] Q. Wei, X. Yang, G. Zhang, D. Wang, L. Zuin, D. Banham, L. Yang, S. Ye, Y. Wang, M. Mohamedi, S. Sun, An active and robust Si-Fe/N/C catalyst derived from waste reed for oxygen reduction, Appl. Catal. B Environ. 237 (2018) 85–93, doi:10.1016/j.apcatb.2018.05.046.
[51] J. Zhang, M. Zhang, Y. Zeng, J. Chen, L. Qiu, H. Zhou, C. Sun, Y. Yu, C. Zhu, Z. Zhu, Single Fe atom on hierarchically porous S, N-codoped nanocarbon derived from porphyra enable boosted oxygen catalysis for rechargeable Zn-air batteries, Small 15 (2019) 1900307, doi:10.1002/smll.201900307.
[52] C. Zhuo, Y.A. Levendis, Upcycling waste plastics into carbon nanomaterials: A review, J. Appl. Polym. Sci. 131 (2014) 1–14, doi:10.1002/app.39931.
[53] X. Wang, Q. Jin, J. Zhang, Y. Li, S. Li, H. Mikulčić, M. Vujanović, H. Tan, N. Duić, Soot formation during polyurethane (PU) plastic pyrolysis: The effects of temperature and volatile residence time, Energy Convers. Manag. 164 (2018) 353–362, doi:10.1016/j.enconman.2018.02.082.
[54] R. Miandad, M.A. Barakat, A.S. Aburiazaiza, M. Rehan, I.M.I. Ismail, A.S. Nizami, Effect of plastic waste types on pyrolysis liquid oil, Int. Biodeterior. Biodegrad 119 (2017) 239–252, doi:10.1016/j.ibiod.2016.09.017.
[55] R. Brandiele, V. Amendola, A. Guadagnini, G.A. Rizzi, D. Badocco, P. Pastore, A.A. Isse, C. Durante, A. Gennaro, Facile synthesis of Pd_3Y alloy nanoparticles for electrocatalysis of the oxygen reduction reaction, Electrochim. Acta 320 (2019) 134563–134572, doi:10.1016/j.electacta.2019.134563.
[56] D. Malko, A. Kucernak, T. Lopes, In situ electrochemical quantification of active sites in Fe–N/C non-precious metal catalysts, Nat. Commun. 7 (2016) 13285–13292, doi:10.1038/ncomms13285.
[57] Q. Wei, G. Zhang, X. Yang, R. Chenitz, D. Banham, L. Yang, S. Ye, S. Knights, S. Sun, 3D Porous Fe/N/C spherical nanostructures as high-performance electrocatalysts for oxygen reduction in both alkaline and acidic media, ACS Appl. Mater. Interfaces 9 (2017) 36944–36954, doi:10.1021/acsami.7b12666.
[58] F. Afsahi, S. Kaliaguine, Non-precious electrocatalysts synthesized from metal–organic frameworks, J. Mater. Chem. A. 2 (2014) 12270, doi:10.1039/C4TA02010C.
[59] A. Gholizadeh, A. Malekzadeh, F. Pourarian, Rapid and efficient synthesis of reduced graphene oxide nano-sheets using CO ambient atmosphere as a reducing agent, J. Mater. Sci. Mater. Electron. 29 (2018) 19402–19412, doi:10.1007/s10854-018-0069-y.
[60] X. Shi, S. Jiang, J. Zhu, G. Li, X. Peng, Establishment of a highly efficient flame-retardant system for rigid polyurethane foams based on bi-phase flame-retardant actions, RSC Adv. 8 (2018) 9985–9995, doi:10.1039/c7ra13315d.
[61] M. Thommes, K. Kaneko, A.V Neimark, J.P. Olivier, F. Rodriguez-Reinoso, J. Rouquerol, K.S.W. Sing, Physisorption of gases, with special reference to the evaluation of surface area and pore size distribution (IUPAC Technical Report), Pure Appl. Chem. 87 (2015) 1051–1069, doi:10.1515/pac-2014-1117.
[62] M. Favaro, L. Perini, S. Agnoli, C. Durante, G. Granozzi, A. Gennaro, Electrochemical behavior of N and Ar implanted highly oriented pyrolytic graphite substrates and activity toward oxygen reduction reaction, Electrochim. Acta. 88 (2013) 477–487, doi:10.1016/j.electacta.2012.10.100.
[63] W.-J. Jiang, L. Gu, L. Li, Y. Zhang, X. Zhang, L.-J. Zhang, J.-Q. Wang, J. Hu, Z. Wei, L. Wan, Understanding the high activity of Fe–N–C electrocatalysts in oxygen reduction: Fe/Fe_3C nanoparticles boost the activity of $Fe–N_x$, J. Am. Chem. Soc. 138 (2016) 3570–3578, doi:10.1021/jacs.6b00757.
[64] H. Okamoto, The C-Fe (carbon-iron) system, J. Phase Equilibria. 13 (1992) 543–565, doi:10.1007/BF02665767.
[65] T. Mineva, I. Matanovic, P. Atanassov, M.-T. Sougrati, L. Stievano, M. Clémancey, A. Kochem, J.-M. Latour, F. Jaouen, Understanding active sites in pyrolyzed Fe–N–C catalysts for fuel cell cathodes by bridging density functional theory calculations and 57 Fe mössbauer spectroscopy, ACS Catal. 9 (2019) 9359–9371, doi:10.1021/acscatal.9b02586.
[66] W. Liu, L. Zhang, X. Liu, X. Liu, X. Yang, S. Miao, W. Wang, A. Wang, T. Zhang, Discriminating catalytically active FeN_x species of atomically dispersed Fe–N–C catalyst for selective oxidation of the C–H bond, J. Am. Chem. Soc. 139 (2017) 10790–10798, doi:10.1021/jacs.7b05130.
[67] U.I. Kramm, M. Lefèvre, N. Larouche, D. Schmeisser, J.-P. Dodelet, Correlations between mass activity and physicochemical properties of Fe/N/C catalysts for the ORR in PEM Fuel Cell via 57 Fe mössbauer spectroscopy and other techniques, J. Am. Chem. Soc. 136 (2014) 978–985, doi:10.1021/ja410076f.
[68] H. Schulenburg, S. Stankov, V. Schünemann, J. Radnik, I. Dorbandt, S. Fiechter, P. Bogdanoff, H. Tributsch, Catalysts for the oxygen reduction from heat-treated iron(III) Tetramethoxyphenylporphyrin Chloride: structure and stability of active sites, J. Phys. Chem. B. 107 (2003) 9034–9041, doi:10.1021/jp030349j.
[69] A. Zitolo, V. Goellner, V. Armel, M.-T. Sougrati, T. Mineva, L. Stievano, E. Fonda, F. Jaouen, Identification of catalytic sites for oxygen reduction in iron- and nitrogen-doped graphene materials, Nat. Mater. 14 (2015) 937–942, doi:10.1038/nmat4367.
[70] J. Li, S. Ghoshal, W. Liang, M.-T. Sougrati, F. Jaouen, B. Halevi, S. McKinney, G. McCool, C. Ma, X. Yuan, Z.-F. Ma, S. Mukerjee, Q. Jia, Structural and mechanistic basis for the high activity of Fe–N–C catalysts toward oxygen reduction, Energy Environ. Sci. 9 (2016) 2418–2432, doi:10.1039/C6EE01160H.
[71] A. Sadezky, H. Muckenhuber, H. Grothe, R. Niessner, U. Pöschl, Raman microspectroscopy of soot and related carbonaceous materials: Spectral analysis and structural information, Carbon 43 (2005) 1731–1742, doi:10.1016/j.carbon.2005.02.018.
[72] R. Kumar, S. Khan, N. Gupta, S. Naqvi, K. Gaurav, C. Sharma, M. Kumar, P. Kumar, S. Chand, Fullerene grafted graphene oxide with effective charge transfer interactions, Carbon 107 (2016) 765–773, doi:10.1016/j.carbon.2016.06.034.
[73] O. Beyssac, B. Goffé, J.-P. Petitet, E. Froigneux, M. Moreau, J.-N. Rouzaud, On the characterization of disordered and heterogeneous carbonaceous materials by Raman spectroscopy, Spectrochim. Acta Part A Mol. Biomol. Spectrosc. 59 (2003) 2267–2276, doi:10.1016/S1386-1425(03)00070-2.
[74] Y. Chen, R. Gokhale, A. Serov, K. Artyushkova, P. Atanassov, Novel highly active and selective Fe-N-C oxygen reduction electrocatalysts derived from in-situ polymerization pyrolysis, Nano Energy 38 (2017) 201–209, doi:10.1016/j.nanoen.2017.05.059.
[75] K. Artyushkova, A. Serov, S. Rojas-Carbonell, P. Atanassov, Chemistry of Multitudinous Active Sites for Oxygen Reduction Reaction in Transition Metal–Nitrogen–Carbon Electrocatalysts, J. Phys. Chem. C. 119 (2015) 25917–25928, doi:10.1021/acs.jpcc.5b07653.
[76] Q. Jia, N. Ramaswamy, U. Tylus, K. Strickland, J. Li, A. Serov, K. Artyushkova, P. Atanassov, J. Anibal, C. Gumeci, S.C. Barton, M.-T. Sougrati, F. Jaouen, B. Halevi, S. Mukerjee, Spectroscopic insights into the nature of active sites in iron–nitrogen–carbon electrocatalysts for oxygen reduction in acid, Nano Energy 29 (2016) 65–82, doi:10.1016/j.nanoen.2016.03.025.
[77] I. Matanovic, K. Artyushkova, M.B. Strand, M.J. Dzara, S. Pylypenko, P. Atanassov, Core level shifts of hydrogenated pyridinic and pyrrolic nitrogen in the nitrogen-containing graphene-based electrocatalysts: in-plane vs edge defects, J. Phys. Chem. C. 120 (2016) 29225–29232, doi:10.1021/acs.jpcc.6b09778.
[78] K. Artyushkova, I. Matanovic, B. Halevi, P. Atanassov, Oxygen binding to active sites of Fe–N–C ORR electrocatalysts observed by ambient-pressure XPS, J. Phys. Chem. C. 121 (2017) 2836–2843, doi:10.1021/acs.jpcc.6b11721.
[79] K.A. Cychosz, R. Guillet-Nicolas, J. García-Martínez, M. Thommes, Recent advances in the textural characterization of hierarchically structured nanoporous materials, Chem. Soc. Rev. 46 (2017) 389–414, doi:10.1039/C6CS00391E.
[80] A. Bonakdarpour, M. Lefevre, R. Yang, F. Jaouen, T. Dahn, J.-P. Dodelet, J.R. Dahn, Impact of loading in RRDE Experiments on Fe–N–C Catalysts: two- or four-electron oxygen reduction? Electrochem. Solid-State Lett. 11 (2008) B105, doi:10.1149/1.2904768.
[81] M. Primbs, Y. Sun, A. Roy, D. Malko, A. Mehmood, M.-T. Sougrati, P.-Y. Blanchard, G. Granozzi, T. Kosmala, G. Daniel, P. Atanassov, J. Sharman, C. Durante, A. Kucernak, D. Jones, F. Jaouen, P. Strasser, Establishing reactivity descriptors for platinum group metal (PGM)-free Fe–N–C catalysts for PEM fuel cells, Energy Environ. Sci. 13 (2020) 2480–2500, doi:10.1039/D0EE01013H.
[82] J. Benson, Q. Xu, P. Wang, Y. Shen, L. Sun, T. Wang, M. Li, P. Papakonstantinou, Tuning the catalytic activity of graphene nanosheets for oxygen reduction reaction via size and thickness reduction, ACS Appl. Mater. Interfaces. 6 (2014) 19726–19736, doi:10.1021/am5048202.
[83] Y. Sun, S. Li, Z.P. Jovanov, D. Bernsmeier, H. Wang, B. Paul, X. Wang, S. Kühl, P. Strasser, Structure, activity, and faradaic efficiency of nitrogen-doped porous carbon catalysts for direct electrochemical hydrogen peroxide production, ChemSusChem 11 (2018) 3388–3395, doi:10.1002/cssc.201801583.